Annu. Rev. Earth Planet. Sci. 1999. 27:385–415

IMPACT CRATER COLLAPSE

H. J. Melosh
Lunar and Planetary Laboratory, University of Arizona, Tucson, AZ 85721;
e-mail: jmelosh@lpl.arizona.edu

B. A. Ivanov
Institute for Dynamics of the Geospheres, Russian Academy of Sciences, Moscow, Russia 117979

KEY WORDS: crater morphology, dynamical weakening, acoustic fluidization, transient crater, central peaks

ABSTRACT

The detailed morphology of impact craters is now believed to be mainly caused by the collapse of a geometrically simple, bowl-shaped "transient crater." The transient crater forms immediately after the impact. In small craters, those less than approximately 15 km diameter on the Moon, the steepest part of the rim collapses into the crater bowl to produce a lens of broken rock in an otherwise unmodified transient crater. Such craters are called "simple" and have a depth-to-diameter ratio near 1:5. Large craters collapse more spectacularly, giving rise to central peaks, wall terraces, and internal rings in still larger craters. These are called "complex" craters. The transition between simple and complex craters depends on $1/g$, suggesting that the collapse occurs when a strength threshold is exceeded. The apparent strength, however, is very low: only a few bars, and with little or no internal friction. This behavior requires a mechanism for temporary strength degradation in the rocks surrounding the impact site. Several models for this process, including acoustic fluidization and shock weakening, have been considered by recent investigations. Acoustic fluidization, in particular, appears to produce results in good agreement with observations, although better understanding is still needed.

INTRODUCTION

It is now generally accepted that impact cratering is an important geological process that has affected the surface of nearly every planet and satellite in the

0084-6597/99/0515-0385$08.00

solar system. Impact craters are nearly ubiquitous landforms on the ancient surfaces of, for example, the Moon, Mercury, and Mars. Even on Earth, with its highly active fluvial and tectonic recycling, some 150 impact craters are currently known (Grieve & Shoemaker 1994). Although nearly all fresh craters can be broadly described as "circular rimmed depressions," the detailed morphologies of impact craters show many variations. The size-morphology progression, first recognized for lunar craters by Gilbert (1893), ranges from small, simple, bowl-shaped craters through craters with central peaks and wreaths of terraces around the rims and up to basins with an internal mountainous ring and, on some bodies, exterior scarps that encircle the impact site.

Currently, it is believed that this morphologic diversity is not a direct result of the crater excavation process but develops only after most of the material has been expelled from the crater. The initial product of crater excavation is believed to be a circular, bowl-shaped cavity with a depth/diameter ratio between 1:4 and 1:3. The form of this initial crater is independent of its diameter, the impact velocity, impact angle (within limits), gravitational acceleration, and nearly every other property of the target or projectile. This "transient" crater then undergoes different degrees of modification as a result of gravitational instability and collapse. The final crater morphology is sensitive to conditions of the target planet, such as the acceleration of gravity, density, and disposition of the surface materials. This study affords both the opportunity of using impact crater morphology to learn about conditions in the target planet and the challenge of understanding how different conditions affect the course of crater collapse.

Transient crater excavation can be treated with relative accuracy using a variety of numerical methods based on a combination of simple Newtonian mechanics and a thermodynamic equation of state (Anderson 1987). Several two- and three-dimensional "hydrocodes" exist that, given simple characterizations of bulk material properties, accurately predict the formation and evolution of the crater formed by a high-speed impact or explosion when gravity is the main factor limiting crater growth. Further research is still needed regarding the role of material strength (or internal friction in granular materials) on limiting transient crater growth.

Crater collapse, however, depends on the essential details of the strength of material surrounding the crater. In particular, standard strength models used in conventional hydrocodes are not successful in describing crater collapse. The rock surrounding the site of an impact is broken, heated, and shaken by the forces that excavate the crater. Such material responds to the differential loads imposed by gravity in ways that are still not fully understood, although it is clear that some type of strength degradation mechanism must temporarily weaken the rock. Indeed, if the target rock retained its static strength properties,

impact craters would not collapse at all, in flagrant contradiction to observations (Dent 1973).

The study of impact crater collapse thus requires a deeper understanding of the fundamentals of dynamic rock failure. A complete understanding of this collapse process does not currently exist. The present challenge in impact cratering studies is to use the observed morphology of extraterrestrial craters and the structure of terrestrial craters to infer the course of events during transient crater collapse. Coupling this phenomenology with a detailed mechanical analysis will, hopefully, bring us closer to a quantitative model for the morphologic variations observed in impact craters.

It may seem incredible that 50 years of study of the impact cratering process have not resulted in a predictive, quantitative model of crater formation. The fact that no such model yet exists, despite many attempts by many authors, indicates that we are still missing major pieces to the puzzle of how rocks respond to sudden shocks. Obviously, such a significant gap suggests that scientific treasures may be gained by further study. In this review we hope to point out the progress that has been made in the past and show some of the promising leads for future work.

IMPACT CRATER MORPHOLOGY

Dence (1965) first classified terrestrial impact craters as either simple or complex in structure. This structural classification, which was based on the study of craters exposed by erosion, also seems to apply to the morphology of fresh craters revealed by images of the surfaces of other planets and satellites. It is worth noting that data sets on terrestrial and planetary craters are highly complementary: because of erosion, geophysical investigations, and direct drilling, the subsurface structure of many terrestrial craters can be explored in detail. The surface morphology, which is usually missing, is often displayed in exquisite detail by images of fresh craters on the surfaces of other planets or satellites.

Simple Craters

Simple craters are circular, bowl-shaped depressions with raised rims and approximately parabolic interior profiles. They exhibit few other internal topographic features with the exception of occasional trails where boulders have rolled from their steep rims into their interiors. The rim-to-floor depths of a large sample of simple craters on the moon are roughly 1:5 of the rim-to-rim diameter (Pike 1977).

Simple craters are widely distributed in the solar system. Most of the craters on small solar system bodies such as asteroids are of this variety. The largest simple crater currently known is 90 km in diameter, on Jupiter's moon Almathea.

Most lunar craters smaller than about 15 km in diameter are simple, as are most terrestrial craters smaller than approximately 4 km in diameter.

Drilling at such simple craters as the 4-km-diameter Brent in Ontario, Canada, reveals a lens of broken rock debris and formerly shock-melted rock underlying the crater floor. This breccia lens in turn lies in a bowl of fractured country rock. The breccia lens thickness is about half of the crater rim-to-floor depth, so the depth from the rim to the bottom of the breccia lens is about one-third of the crater diameter. The volume of the breccia lens is roughly one-half the volume of the crater itself.

The distribution of melt in the breccia lens suggests that the lens is created by the collapse of the steep outer walls of the transient crater (Grieve et al 1977). The breccia lens at Meteor Crater, Arizona, is a mixture that contains clasts from all of the rock units intersected by the crater (Shoemaker 1963), suggesting that the debris first surged outward along the wall of the growing cavity and then drained back into the crater interior.

These facts indicate that a simple crater forms by the relatively straightforward collapse of the rim of the transient crater immediately after it forms. Because the rim is composed of broken rock debris and forms close to the angle of repose of loose rock debris, this process is mechanically plausible and does not present any special difficulties to understand or analyze.

Complex Craters

Complex craters, as their name implies, possess a much more complicated structure than simple craters. On Earth they exhibit central structural uplifts, rim synclines, and outer concentric zones of mainly normal faulting. Images from spacecraft show extraterrestrial craters with single or multiple central peaks, flat inner floors, and terraced rims. The depths of complex craters increase with increasing diameter, but they increase much more slowly than the depths of simple craters. Pike (1977) showed that the depths of complex lunar craters increase as approximately the 0.3 power of their diameter, a result consistent with the depths of complex craters on Mercury and Venus (McKinnon et al 1997).

Complex craters range in diameter from a few kilometers on Earth to a monster crater on asteroid 4 Vesta that is 460 km across, so large that its rim almost encircles the 530 km-diameter equator of Vesta, although its central peak juts out of Vesta's south pole (Thomas et al 1997). Even the icy satellites exhibit this type of crater. In addition to the many complex craters on Ganymede and Callisto, the 130 km-diameter "death star" crater Herschel on Saturn's moon Mimas is a classic complex crater, as is the isostatically relaxed 400 km-diameter crater Odysseus on Tethys. Recent Galileo images indicate that the 25 km-diameter crater Cilix on Europa is also a classic complex crater.

The transition between simple and complex craters occurs over a relatively narrow diameter range on any given solar system body and seems to scale as the inverse power of the surface gravity, g. Thus, the simple-complex transition is relatively well determined on the Moon at about 15 km diameter. On Mercury and Mars the transition occurs at about 7 km diameter, and on Earth it drops to 3 to 5 km diameter (the diameter range seems to depend on whether the crater forms in sedimentary or crystalline rocks). The large crater on Vesta corresponds in nearly every way to a gravity-scaled 62 km-diameter crater on the Moon (Thomas, et al 1997). With Vesta's low surface gravity of 0.22 m s^{-2}, the $1/g$ relation is extended to approximately more than two orders of magnitude in gravitational acceleration.

The simple-complex transition has not been determined accurately for the icy satellites around Jupiter and beyond because Voyager images lack sufficient resolution to accurately determine the depths of small craters. Early studies (Schenk 1991) suggest that the transition takes place at much smaller diameters on icy satellites than on silicate bodies. Thus ice appears to be weaker, in some sense, than silicates, but the exact quantification of this result must await analysis of the high-resolution Galileo data.

As crater size on any one body increases further, the central peak complex in a complex crater begins to break up and form an inner ring of mountains. In sufficiently large craters the ring appears at about one-half the rim diameter. Such craters are termed "peak ring" craters and have been observed on Earth, Venus, Mars, Mercury, and the Moon (Melosh 1989). Study of large Venusian craters shows that this transition is actually gradual (Alexopoulos & McKinnon 1994), with a small inner ring expanding to half of the rim radius as the crater diameter increases. The transition between central peak and peak ring craters also appears to scale as $1/g$, although the range of g for which we have data is more limited than for the simple-complex transition. Peak rings are uncommon on icy satellites: their place in the size-morphology sequence is taken by central pit craters, whose formation may be related to the unusual properties of water ice (Schenk 1993), but is otherwise not understood at the present time. Central pit craters also occur on Mars.

Multi-Ring Basins

The very largest impact craters on some bodies exhibit many more rings. The classic basin is Orientale, just over the Moon's western limb. First recognized on rectified lunar photographs in 1962 (Hartmann & Kuiper 1962), Orientale possesses at least five circular rings that form inward-facing scarps up to 6 km high. A second variety of multi-ring basin was discovered on the Jovian satellite Callisto during the Voyager encounters in 1979–1980 (Passey & Shoemaker 1982). Typified by the Valhalla structure, this type of multi-ring basin exhibits

a central bright patch surrounded by a system of concentric ridges. These ridges are surrounded by dozens of grabens or outward-facing rings that may extend thousands of kilometers from the impact point. Multi-ring basins of both types appear to form as a tectonic response of the target's lithosphere to the cavity created by the impact (Melosh & McKinnon 1978, McKinnon & Melosh 1980). As such, the formation of multiple rings indicates the presence of a low-viscosity or low-strength layer below the surface. The extent of the ring system provides an indication of the strength and thickness of the lithosphere, with extensive rings forming in thin, weak lithosphere (Melosh 1982b).

Not all planets possess multi-ring basins. Despite some assertions to the contrary (Spudis 1993), it does not appear that any crater on Mercury possesses an external ring scarp (Wood & Head 1976), even including the 1300 km-diameter Caloris basin. The Moon possesses about nine multi-ring basins, and Venus supports four multi-ring basins (Alexopoulos & McKinnon 1994). The 180 km-diameter Chicxulub impact crater on Earth is now definitely identified as a multi-ring basin (Morgan et al 1997), and more circumstantial evidence suggests that the 200 km-diameter Sudbury structure might also be a multi-ring basin (Spray & Thompson 1995). The case for Mars is less clear because of erosion: neither the 2000 km-diameter Hellas basin nor the 1200 km-diameter Argyre basin shows multi-ring scarps. The highly degraded impact structure Isidis may have rings at 1100 and 1900 km diameter (Wood & Head 1976), but interpretation is hampered by extensive postimpact alteration. Ganymede possesses both an Orientale-type basin in the 550 km-diameter ring around the crater Gilgamesh and evidence for an enormous Valhalla-type structure in the furrows that cross Galileo Regio (Schenk & McKinnon 1987). Besides Valhalla itself, Callisto also possesses at least two other smaller structures of the same type. The recent Galileo images of Europa have revealed two classic Valhalla-type structures, Callanish and Tyre, neither of which is more than about 40 km in diameter.

Multi-ring basins are apparently formed by a type of collapse qualitatively different from the collapse that yields complex central peak or peak ring craters. The transition to multi-ring scarps does not scale as $1/g$ and seems to depend a great deal on the rheological conditions near the surface of the planet on which they form (specifically, a weak subsurface layer that can flow on the timescale of crater collapse). For these reasons, and in the interest of brevity, we exclude multi-ring basins from further consideration in this review, referring the reader to Melosh (1989, chapter 9). There is still a great deal of controversy about how these largest of impact structures form, and much work remains to be done before their formation is fully understood.

MECHANICS OF IMPACT CRATER FORMATION

Principal Stages of Impact Crater Formation

The impact process as a whole can be described as a kind of explosion, in which the initial kinetic energy of the projectile does work on the target to create a hole—the crater—as well as heating the material of both projectile and target. In most cases of planetary interest, the crater is much larger than the original projectile.

The course of events in a high-velocity impact may be separated into several sequential stages. Each of these stages is dominated by a specific set of major physical and mechanical processes. It is conventional to distinguish three main stages of an impact event (Melosh 1989). These stages are contact and shock compression, transient cavity growth by crater material ejection, and, finally, transient cavity modification (slumping or collapse). These stages do not have strict boundaries and are used for convenience in the analysis of impact processes because they highlight the dominant mechanisms acting at any given time.

Although the first stage, contact and compression, has little to do directly with crater collapse, it lays the foundation for the subsequent crater formation events, so we begin with a brief description of this stage. The subsequent stages of crater excavation and modification will be discussed in more detail.

Contact and Compression—Shock Wave Generation

In the first stage of an impact the energy released by deceleration of the projectile results in the formation and propagation of shock waves away from the point of impact. A shock wave propagates through the projectile and into the target. This results in a redistribution of the projectile's initial kinetic energy into kinetic and internal energy of all colliding material. The residual kinetic energy is spent ejecting material and opening the transient cavity. The internal energy heats both the projectile and target. For sufficiently strong shock waves this may result in melting or vaporization of material near the impact site.

Contact and compression compose the briefest of the three main stages, lasting only as long as it takes the projectile to enter the target and deposit its energy. If the projectile is approximated as a sphere of radius a that strikes at velocity v and at an angle to the horizontal θ, the duration of this stage is given by $t_{cc} = a/(v \sin\theta)$. For a typical 1 km-diameter impactor striking at 15 km s^{-1} and a 45° angle, this stage lasts literally for only the blink of an eye—about 0.1 seconds.

During this stage, shock pressures are of the order of the stagnation pressure ρv^2, where ρ is the smaller of either the projectile or target density. At speeds

above a few kilometers per second these pressures greatly exceed the strengths of any known materials, and the process can be treated hydrodynamically.

Owing to the rapidly changing geometry of the projectile and target during this stage and the highly nonlinear equations of state that must be used to describe the thermodynamic properties of common materials at high pressure and temperature, contact and compression must be studied numerically. Fortunately, numerical hydrocodes are now highly developed for both two-dimensional (axisymmetric, corresponding to vertical impacts) and three-dimensional (required for oblique impacts, which may possess only bilateral symmetry) geometries (Johnson & Anderson 1987). Full three-dimensional computations at high resolution still tax modern computers but are now well within the range of solution on workstation-class machines.

Excavation and Transient Crater Growth

After the shock wave forms in the target it expands away from the impact site, compressing and accelerating the material it encounters. Although the pressure drops toward zero after the shock wave passes, the particle velocity drops to about 1/5 of the peak velocity in the shock wave. This residual velocity, the existence of which is attributed to the thermodynamic irreversibility of the shock wave, eventually acts to open the crater (Melosh 1985).

In the first moments after the shock passes over it, material in the target moves outward along directions that are approximately radial to the point of impact. Because of the presence of the target's free surface, however, pressure gradients behind the shock tend to deflect the particle trajectories toward the surface. The mutual action of these pressure gradients and the inertia of the initial pulse motion result in curved trajectories of target material. The complex material motion away from the point of impact opens the growing cavity, the "transient crater." Roughly equal volumes of material are either ejected ballistically from the crater or displaced by plastic flow downward into the target. In most experimentally and numerically modeled impacts the growing transient crater is initially shaped like a hemisphere. Owing to greater resistance with increasing depth in nonductile targets, the transient crater's depth stops growing at a time when the crater radius continues to increase. The transient cavity eventually reaches a maximum volume. This moment may be defined as the effective time of transient cavity formation (Melosh 1989).

The general timescale for the growth of a transient crater is defined by the basic principles of mechanics: a high-velocity impact transfers a specific amount of energy and momentum into the target material. In response, the material begins to move ("to flow") away from the point of impact. This motion is essentially an inertial one: the transfer of energy and momentum from the shock waves to the target occurs very quickly in comparison to the time of the

cratering excavation flow. The initial kinetic energy of the cratering flow is spent working against strength or friction forces and gravity. The simple balance of these factors allows us to integrate the equation of motion and to estimate the moment when the excavation flow should stop.

Thus, if the transient crater growth is halted by gravity alone, as would be the case for impacts into liquid water, the timescale is of order $\sqrt{H_f/g}$, where H_f is the final crater depth and g is the acceleration of gravity. If crater growth is halted by elastic-plastic material strength Y, the timescale is given by $H_f\sqrt{Y/\rho}$. For more complicated failure laws or more accurate estimates of excavation time, detailed numerical studies with more elaborate material models are required.

The maximum depth and diameter of the transient crater are determined by the properties of the target, which may include density, strength, and acceleration of gravity. On the other hand, the ratio of depth to diameter seems to be nearly independent of size, strength, gravity, etc. Although some early centrifuge experiments and numerical computations suggested that large transient craters might be shallower than small ones, there is no longer support for this theory (O'Keefe & Ahrens 1993). Very recent studies of the crustal thickness beneath large lunar basins also support this hypothesis of "proportional scaling" for the dimensions of the transient crater up to craters at least 500 km in diameter (Wieczorek & Phillips 1998). For complex craters the validity of proportional scaling does not, however, imply that at some single point in time the crater had the form of a bowl-shaped depression with depth-to-diameter ratio of 1:3 to 1:4. In many simulations the floor of the transient crater achieves its maximum depth and begins to rise into a central peak while the diameter is still increasing (Melosh 1989).

The size of the transient crater can be estimated by a variety of methods, ranging from laboratory-scale experiments, numerical computations, and, most conveniently, scaling laws. The use of scaling laws for estimating the size of impact craters has reached a high level of sophistication (Holsapple & Schmidt 1982). Based on the idea that early-time phenomena described by projectile parameters are related to late-time cratering phenomena by a single, dimensional, "coupling constant," scaling laws link nondimensional crater descriptors by a variety of power laws. For well-studied cases such as impacts into water or into ductile metals whose strength is described by an elastic-plastic yield law, scaling relations give accurate descriptions of the overall dimensions of the transient crater (Holsapple & Schmidt 1982, O'Keefe & Ahrens 1993).

Although the strength of materials such as water (strengthless) or ductile metals seems to be reasonably well understood, the strength response of brittle materials such as rock or ice is much less clear. Ductile metals have nearly the same strength Y in tension as in compression, whereas rock is much weaker

under tension than under compression. One consequence of this dependence of strength on pressure is that sufficiently large impacts may shatter the rock in tension long before the crater has time to grow, effectively destroying any strength the target rock may possess long before the crater opens. Asphaug & Melosh (1993) noted this effect in a study of the formation of the Stickney crater on Phobos. In this computation of an impact on an initially strong basalt (or ice) asteroid, the outward radial displacement of the target just behind the shock wave produced strong hoop tension that shattered the rock shortly after it was released from compression. This effect has also been observed experimentally in explosions on transparent media (Fourney et al 1984).

Target strength degradation by stress waves was studied in more detail by Nolan et al (1996), who concluded that, for craters on large bodies such as Earth, any intrinsic target strength was destroyed by tensile failure in craters produced by projectiles larger than a few meters in diameter. Transient crater growth in these cases proceeds in a mass of shattered rock, and, although rock friction may play a role in reducing crater size (Ivanov & Kostuchenko 1998), strength probably does not. Much more work needs to be done before the role of rock strength is fully understood, but it appears that the assumption long recommended by such crater-scaling experts as Schmidt & Housen (1987), of transient crater growth in a strengthless medium, may give the best approximation to the truth. Further work should concentrate on the mechanism of strength degradation and how to incorporate this mechanism in the growth of the transient crater.

Elastic Rebound

For many years, geologists used the terms “rebound” or “elastic rebound” to describe their observations in terrestrial impact structures. However, the exact mechanical nature of this phenomenon was not discussed in detail. From the detailed study of underground nuclear explosions and small-scale laboratory explosion experiments it is known that, far enough from the explosion point, rocks are not crushed but instead respond elastically to applied forces. This elasticity causes the distant rocks to experience only reversible deformation: after the explosion impulse, they return to their pre-event state. Such reverse motion of material caused by rebound in the elastic zone has been documented by experiments on contained explosions (Rodionov et al 1971).

In cratering events the presence of the free surface decreases the rebound amplitude in comparison to that observed in underground explosions because the deformational rebound of the elastic zone tends to be discharged in the direction of the free surface. Ivanov et al (1982) conducted experiments with an exotic target material consisting of small pieces (0.5 to 0.8 mm) of rubber. Mixtures of this “granulated” rubber with sand and chalk permitted control

of the interparticle friction. Explosion cratering in this medium showed very strong true elastic rebound, producing a central peak in a crater only 20 cm in diameter. However, it is unclear how to scale these experiments to events several kilometers in size.

Numerical simulations also permit investigation of this elastic rebound. Ivanov and Kostuchenko (1998) presented results from a pure Lagrangian calculation of a 5 km s^{-1} impact into a rock target at a scale corresponding to a 40 km-diameter impact crater. The rebound of the elastic zone is obvious, but the maximum rebound velocity was only about 50 m s^{-1}. If the surface rocks were launched vertically at this velocity, they could rise only approximately 125 m. This is not sufficient to uplift the crater floor substantially in a crater of this size (Figure 1), for which the expected uplift is about 4 km (Equation 1b). One may suppose that a 50 m s^{-1} rebound could be enough to make a detectable uplift in craters of smaller scale. However, for smaller-scale events the role of lithostatic pressure, which keeps the rocks in an elastic state, is also decreased, and the damaged zone increases in size (Dabija & Ivanov 1978, Ivanov et al 1997). The larger relative size of the damaged zone decreases the role of the elastic rebound. Elastic rebound has been observed in experimental explosive cratering (Ullrich et al 1977) but only in specialized circumstances involving very strong rocks.

Although elastic rebound is not affected directly by gravitational acceleration, it is difficult to see how the various morphometric transitions in impact craters can be a simple inverse function of g unless gravity, not elastic forces, controls the process. The systematic change of crater morphology with increasing size (simple bowl-shaped to central peaked to double ringed) is found on all planetary bodies with a solid crust. For terrestrial-type planets (Mercury, Venus, Earth, the Moon, Mars and, now, the asteroid Vesta) the critical diameters of these morphological changes are inversely proportional to the surface gravity (Pike 1980). This strongly supports the idea that gravity is the main force driving transient crater collapse. We will henceforth neglect the role of elastic rebound in most large impact events, but it may play some role in special circumstances.

Modification of the Transient Crater

In most large craters, the modification or collapse of the transient cavity produces the final crater shape. The ultimate driving force is gravity: transient crater collapse results in a shallower crater geometry that is more stable in a gravity field (Quaide et al 1965). Depending on the size of the cratering event, modification may include the slumping of the crater walls in the form of landslides, stepped terrace formation, uplift of the crater floor, and central peak formation. The inward and upward material motion during the modification stage results in a complex intermixture of breccia and impact melt inside the crater

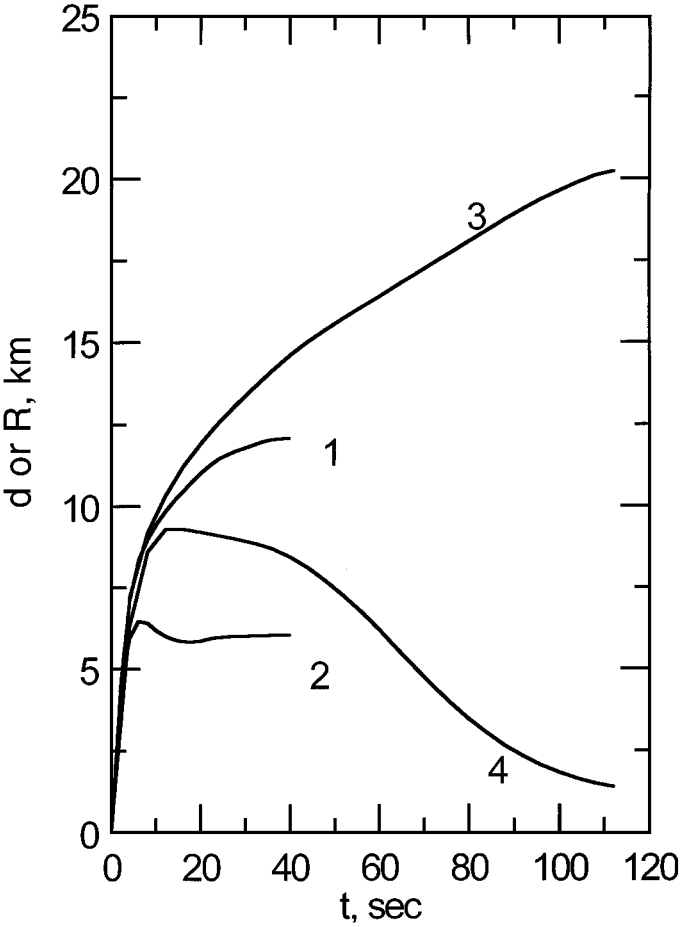

Figure 1 Crater radius and depth versus time for the vertical impact of a projectile with an impact velocity of 5 km s^{-1} and a diameter of 6 km in a terrestrial gravity field. Curves 1 and 2 show radius and depth, respectively, for dry friction. Curves 3 and 4 show radius and depth, respectively, for a model of acoustic fluidization. An elastic rebound for the case of dry friction is seen at $t = 8$ s (curve 2). Note the drastically increased transient depth owing to acoustic fluidization. After Ivanov & Kostuchenko (1997).

depression. The mechanical style of modification depends on the gravity field of the planet and the strength of near-surface rocks. A full mechanical model of crater collapse is still under construction. However, it is clear that to explain the observed dependence of final crater morphology on crater diameter (ranging from simple craters to craters with a central peak to double-ring craters), some type of extreme strength degradation must occur in the rocks surrounding the crater. One very specific (and perhaps somewhat exotic) mechanism that has been proposed is acoustic fluidization (Melosh 1979, 1989, Ivanov & Kostuchenko 1997). Another model that is patterned after thermal weakening of metals (see below) is by O'Keefe & Ahrens (1993, 1998).

FORMATION OF SIMPLE CRATERS

In media such as ductile metals, plasticene, or wet clay, plastic flow occurs after the deviatoric stresses exceed some threshold *Y*. This flow does not dramatically change the final shape of the transient cavity. So long as gravitationally induced stresses following excavation do not exceed the yield stress *Y*, the shape of craters in these materials remains close to a hemisphere. Thus the main morphometric parameter, the ratio of crater depth to crater diameter, is close to 1:2. Craters of this kind, commonly produced at laboratory scales, can be conveniently thought of as "frozen" transient craters.

In media such as sand or fragmented rocks, two mechanisms modify the transient cavity shape. The first mechanism is dry friction: the action of dry friction leads to the continued growth of the transient cavity diameter after the moment when the cavity depth reaches its final value. The second mechanism is the slumping of the steep transient cavity walls under the action of gravity. These two mechanisms result in similar crater shapes that are close to a paraboloid of revolution with a depth-to-diameter ratio in the range from 1:5 to 1:4. Both mechanisms generally act together, but typically dry friction is more important in laboratory-scale impact and 0.1- to 1-m-diameter explosion craters. Small lenses of mixed breccia produced by wall slumping appear in missile impact craters in the size range of 2 to 10 m on Earth (Moore 1976). Wall slumping dominates for natural craters with diameters above approximately 100 m.

Wall slumping is the main modification process for simple craters. The result of slumping is a breccia lens that overlies the true floor of the crater. Grieve & Garvin (1984) developed a qualitative model of the mass balance attributed to crater wall slumping. The true floor is the remnant of the transient cavity floor, and it may be recognized by the presence of melted rock that once lined the transient crater and by the fractured but unmixed rocks beneath. For example, Arizona's well-known Meteor Crater, with a diameter of 1.2 km, has a depth

from the level of the preimpact surface to the true floor (called true depth) of approximately 300 m (true depth-to-diameter ratio of 1/3). The true floor is covered with a 150 m-thick breccia lens. The resulting apparent depth of the crater is $(300 - 150) = 150$ m below the original target surface. Finally, the ratio of the crater depth measured from the uplifted rim crest to the visible (apparent) crater floor of Meteor Crater is 0.19 (Roddy et al 1975).

FORMATION OF COMPLEX CRATERS

Complex craters have smaller depth-to-diameter ratios than simple craters. The geological study of terrestrial complex craters shows that rock strata beneath the center of the crater are uplifted above the pre-impact level (Dence et al 1977). At the center of such a crater this uplift creates a central mound or central peak. A ring depression (or circular trough or rim syncline) surrounds the central mound. This ring depression is filled with fragmented material (allogenic breccia) and impact melt. On other planets one can see only the summit of the central mound rising above a relatively level plain that is underlain by a mixture of breccia and melt. The central mound is a manifestation of the main modification mechanism for complex crater formation: the uplift of the transient cavity's floor. This uplift is accompanied by subsidence of the crater rim. Overall, the process is referred to as transient crater collapse.

MECHANICS OF TRANSIENT CRATER COLLAPSE

Uplift of Deep Strata

Numerous observations of the geology of complex terrestrial impact craters demonstrate that deep target strata are uplifted above the pre-impact level due to the collapse of the transient cavity. In some cases the boundary between sedimentary and basement rocks traces this uplift. Eroded impact structures clearly expose deep layers of basement rocks (for example, at Puchezh-Katunky and Kara in Russia or Vredefort in South Africa). For impact craters entirely formed in sedimentary targets (for example, Steinheim in Germany and Gosses-Bluff in Australia) one can trace the structural uplift using identifiable horizons of different kinds of sedimentary rocks.

Grieve et al (1981) summarized geological and geophysical stratigraphic data on the structural uplift with

$$SU = 0.06D^{1.1} \tag{1a}$$

where SU is the stratigraphic uplift (km) and D is the final crater diameter (km). The data set used here includes 14 structures from 3 to 30 km in diameter

and the deeply eroded Vredefort structure. Without the point for Vredefort the data for 14 craters may be also presented as

$$SU = 0.1D \tag{1b}$$

to the same level of accuracy (Ivanov et al 1982, Basilevsky et al 1983).

An independent estimate of the stratigraphic uplift may be derived from the observations of unmelted shocked rocks in the central uplift. Rocks in the central uplifts of terrestrial craters exhibit a level of shock metamorphism characteristic of shock pressures from 30 to 50 GPa. This is well below the melting pressure for typical crustal materials. The physics of high-velocity impacts indicate that this range of pressure is much less than the maximum pressure during contact and compression. Consequently, the presence of these rocks close to the surface shows that they were shocked at greater depth and then uplifted to their present position during crater modification. The depth at which the shock pressure falls to 30 to 50 GPa gives an independent estimate of the stratigraphic uplift. Not surprisingly, this estimate is close to that derived from the geological data in Equations 1a and 1b (Ivanov et al 1982, Basilevsky, Ivanov et al 1983).

Timescale of Crater Collapse

Observational data on the geology of terrestrial craters give some limits on the timescale for complex crater formation. In most known terrestrial craters, overlying sediments younger than the crater itself are not deformed. This means that the crater modification time is short in comparison with the rate of accumulation of sediments. In some craters the presence of a massive impact melt sheet is well documented. The best examples are Boltysh (Ukraine, $D = 25$ km) and Manicouagan (Quebec, Canada, $D \sim 70$ km). In both cases the impact melt sheet surrounds the central uplift (Onorato et al 1978, Masaitis et al 1980). If the melt sheet had solidified before the central mound formed, the uplift should deform the impact melt sheet. In contrast, the observed geology corresponds far better to melt solidification after the central mound formed. Thus the impact melt solidification time gives an upper limit to the duration of central uplift formation.

Impact melt solidification is not, unfortunately, a simple process. Impact melts differ sharply from "normal" volcanic melts in two respects: (*a*) the wide range of initial temperatures ranging from the melting point to the boiling point (volcanic melts are mostly separated at the liquidus), and (*b*) the widely variable clast content, which is a result of mixing by the flow during crater excavation. Based on investigations of the Manicouagan melt sheet (Onorato et al 1978), the cooling history of this massive impact melt consists of two main phases. In the first phase, local heat exchange (millimeter to centimeter scale)

results in the attainment of a local temperature equilibrium between melt and clasts. In most cases the temperature drops down to the liquidus in 100 seconds. After the first 100 seconds the impact melt viscosity becomes relatively large—some big boulders may be trapped before they reach the melt pool bottom. The local thermalization time depends on the clast temperature. On Venus the local thermalization time may be 10 times longer than on Earth due to Venus' inherently high crustal temperature (Ivanov et al 1992).

In the second phase of melt cooling (after local thermalization is complete), thermal conductivity controls the cooling rate of the entire mass. The thicknesses of hot melt/suevite bodies vary widely (suevite is the name given to a mixture of clasts and a quantity of impact melt). In the range of crater diameters from 10 to 100 km, this thickness h ranges from 200 m to 2 km. The cooling time of such a mass is given by the simple formula $t^* \sim h^2/\kappa$, where κ is the thermal diffusivity and t^* is the characteristic cooling time. For a typical rock, κ is of order $10^{-6}\,\mathrm{m^2\,s^{-1}}$, and for h of 1 km, $t^* \sim 3 \times 10^4$ years. So 30,000 years is a first-order estimate for a 1 km layer, and it varies as h^2. This estimate may be dramatically changed by water circulation where conduction is outstripped by hydrothermal heat transfer.

The first phase of melt cooling establishes the best limit on the timescale for crater collapse. Since the viscosity of the melt mass increases greatly after local thermalization, it is clear that the central uplift in both Boltysh and Manicouagan craters formed within about 100 seconds of their excavation. Young lunar craters such as Copernicus and Tycho also exhibit flat, locally irregular floors that are believed to represent solidified impact melt units. Because these floors lap up against both central peaks and terraces in the outer walls, their solidification must postdate most of the crater collapse process.

A minimum timescale for transient crater collapse may be derived from the collapse of a crater in a strengthless, inviscid fluid. Numerical calculations as well as laboratory experiments give a timescale of the order of $\sqrt{H_f/g}$, where H_f is the maximum transient cavity depth. For transient depths in the range of 1 to 10 km (final crater diameter range 10 to 100 km) the gravity collapse time is 10 to 30 seconds. This is also approximately the same time required for the transient cavity to attain its maximum depth in a strengthless target.

By comparing all these estimates, we see that for strengthless targets the transient cavity has enough time to collapse and to form a prominent central uplift before the solidification of impact melt (timescale of several minutes). The subsequent cooling of melt/suevite bodies occurs over a timescale of thousands of years.

On a still longer timescale, slow viscous relaxation of a crater that is initially out of isostatic equilibrium will flatten it still further. The viscous (creep)

relaxation time t_R is given roughly by

$$t_R = \frac{4\pi\eta}{\rho g D} \tag{2}$$

where η is an effective target viscosity, ρ is the target density, g is the acceleration of gravity, and D is crater diameter (Scott 1967). Upper crustal rocks on silicate planetary bodies have viscosities well above 10^{25} Pa s, so for craters with diameters in the range 10 to 100 km the viscous relaxation time is in the range of 10^{10} to 10^9 years. This time is comparable to or much larger than the age of the Solar System. Viscous relaxation may occur faster on bodies whose surface rocks are closer to their melting points or in craters that are large enough to respond to the flow of rocks deep in the interior of a planet. One of the best examples of a viscously relaxed crater is Odysseus on Tethys.

Gravity Collapse: Strength Properties, Friction, Thermal Softening, and Creep

As described, in large-scale events, gravity collapse results in uplift of the crater floor in place of (or in addition to) a simple landslide from the wall. This phenomenon is what one observes during cratering in water or milk (Worthington 1963) or any strengthless fluid. The analogy with a fluid was widely used to create a set of "splash" or "tsunami" models of complex crater formation (see e.g. Baldwin 1981). Quantitative analyses of transient cavity collapse in a gravity field show, however, that the process is better described by the collapse of a crater in a material that behaves as a Bingham fluid. This type of rheology has also recently been found to provide an excellent phenomenological description of the flow of large masses of rock debris in large rock avalanches (Dade & Huppert 1998).

A Bingham fluid responds elastically to an applied stress until some strength limit is reached, the "Bingham yield stress" Y_B, after which it flows as a viscous fluid (Bingham 1916). Although it was initially unclear just how this peculiar rheology is realized in the rock surrounding an impact event, Melosh (1977) showed that the observed morphology of collapsed craters is well described by a fluid with a Bingham yield stress. The required yield stress is in the vicinity of 30 bars and must be accompanied by an effective angle of internal friction below five degrees (McKinnon 1978). This model is also quantitatively consistent with the formation of slump terraces in lunar (Pearce & Melosh 1986) and Mercurian craters (Leith & McKinnon 1991). The assumption of an appropriate viscosity even gives a quantitative explanation of how peak rings form, by sloshing of the fluidized debris surrounding the transient crater (Melosh 1982a, Alexopoulos & McKinnon 1994).

In spite of the great difference between the behavior of a Bingham fluid and the familiar static rheology of rock material (Jaeger & Cook 1969), the Bingham rheology does seem to provide a good phenomenological description of the behavior of rock debris in the vicinity of an impact (Melosh 1989). Because the rock debris needs to exhibit this strange behavior only for as long as the crater takes to collapse, we seek a mechanism that causes only temporary fluidization. The nature of this fluidization is poorly understood at present (see the review of hypotheses, Melosh 1989). Melosh (1979) suggests that this fluidization is fundamentally caused by acoustic waves (strong vibrations) in the broken rock debris surrounding the freshly excavated crater. This approach is discussed further in the next section.

Although agreeing that strength degradation is necessary to correctly model crater collapse, O'Keefe & Ahrens (1993, 1998) propose a model apparently inspired by existing models for thermal weakening of metals. Numerical hydrocode modelers have long recognized that, as the melting point of a material is approached, its strength must decrease toward zero (Anderson 1987). A standard procedure is to multiply the elastic-plastic yield strength Y by a factor proportional to $(1 - E/E_m)^n$, where E_m is the internal energy at melting (hydrocode computations do not yield temperature directly; they yield only internal energy, which is the reason for this representation), and E is the specific internal energy of the material. The exponent n is usually taken as either 1 or 2. O'Keefe & Ahrens (1993), using $n = 1$, replace E_m with a new energy E_{sw} that is about two orders of magnitude smaller than E_m. E_{sw} is interpreted as the energy necessary for shock waves to shatter the rock. Thus, they are able to derive the same threshold for the simple to complex transition as derived by using the Bingham model discussed above, with the same $1/g$ dependence on surface gravity, although the spatial distribution of strength is different in the two models, as is the dependence on crater size.

The main mechanism investigated numerically by O'Keefe & Ahrens (1993, 1998) is the shock heating of the target material and the corresponding decrease of strength. Thermal softening is especially efficient for large-scale events: whereas gravity tends to decrease the transient cavity size in large events, the zone of intensive shock heating becomes larger in comparison with the zone of the excavation flow. Scaling laws show that the excavation volume for a terrestrial crater with a diameter of 300 km is approximately equal to the impact melt volume (p. 123 and Fig. 7.7, Melosh 1989). However, for smaller craters ($D < 200$ km), shock heating seems to influence too small a volume, and the flow of relatively cold rocks must control the excavation and modification stages of impact cratering.

Ivanov & Deutsch (1998) constructed a numerical model of the Sudbury impact crater's formation. They used a thermal-softening strength model for the

rock target similar to the model used by O'Keefe & Ahrens (1993, 1998). In addition, Ivanov et al (1996) introduced a typical continental geotherm in the target. Nevertheless, the results for a Sudbury-scale event show that dry friction dominates the modification of the transient cavity. With thermal softening alone, the simulations show an avalanchelike collapse of the transient crater walls. Crater floor uplift was the main form of modification only when the friction coefficient was artificially decreased (Figure 2). The magnitude of this friction reduction is comparable with values previously estimated by McKinnon (1978). One possible mechanism for this friction reduction is discussed in the next section.

ACOUSTIC FLUIDIZATION

Original Model

Melosh (1979) originally proposed his model as a short-wavelength extension of existing models of earthquake-induced landsliding (Seed & Goodman 1964). It was well known that explosions (and, by extension, impacts as well) induce strong ground motions (Cooper & Sauer 1977). Analysis of a series of 10-ton TNT explosion tests revealed stress fluctuations exceeding the overburden stress near the crater (Gaffney & Melosh 1982). This suggested that the strong shaking produced during crater excavation might play a major role in affecting the rheology of the debris surrounding the crater (Melosh & Gaffney 1983).

The fundamental idea of acoustic fluidization relies on the fact that for a coulomb material the yield stress is, to first order, a linear function of the overburden pressure with a proportionality coefficient μ, the coefficient of internal friction. Portions of the material that are normally under too high an overburden pressure to fail may nonetheless flow plastically if the ambient vibrations temporarily reduce the overburden pressure below the coulomb threshold. Note that, in this context, "acoustic" refers to elastic (sound) waves in the rock debris, not in any adjacent atmosphere.

The strain rate $\dot{\varepsilon}$ in acoustically fluidized debris is given by a rather complicated function of applied shear stress τ, overburden pressure p, and the variance of the pressure fluctuations σ. By following common engineering practice (Crandall & Mark 1973), the amplitudes of the pressure fluctuations are assumed to be distributed according to a Gaussian law. The strain rate also depends on the density of the debris ρ, the *S*-wave velocity in the debris β, and the dominant wavelength of the acoustic field λ. In terms of these variables the strain rate of vibrated granular debris is

$$\dot{\varepsilon} = \frac{\tau}{\rho\lambda\beta}\left\{\frac{2}{\operatorname{erfc}[(1-\Omega)/\Sigma]} - 1\right\}^{-1} \tag{3a}$$

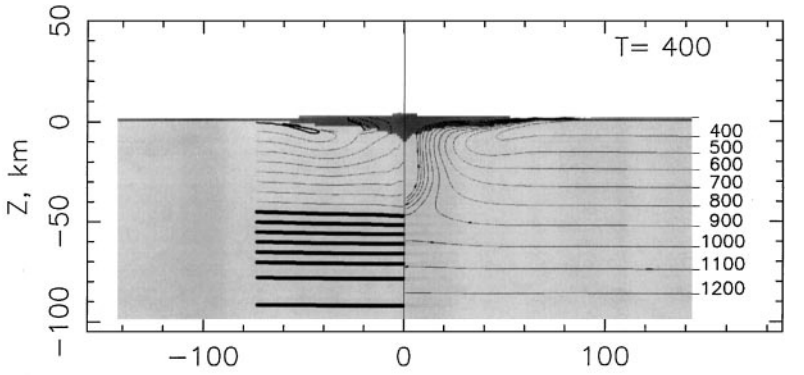
T= 400
Z, km
50
0
−50
−100
−100
0
100
400
500
600
700
800
900
1000
1100
1200

(a)

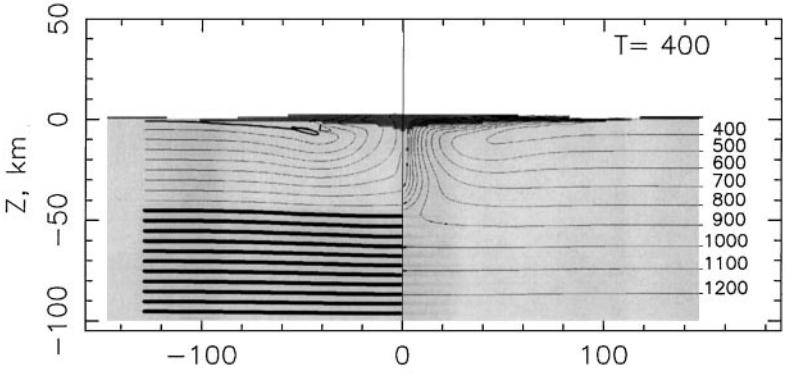
T= 400
Z, km
50
0
−50
−100
−100
0
100
400
500
600
700
800
900
1000
1100
1200

(b)

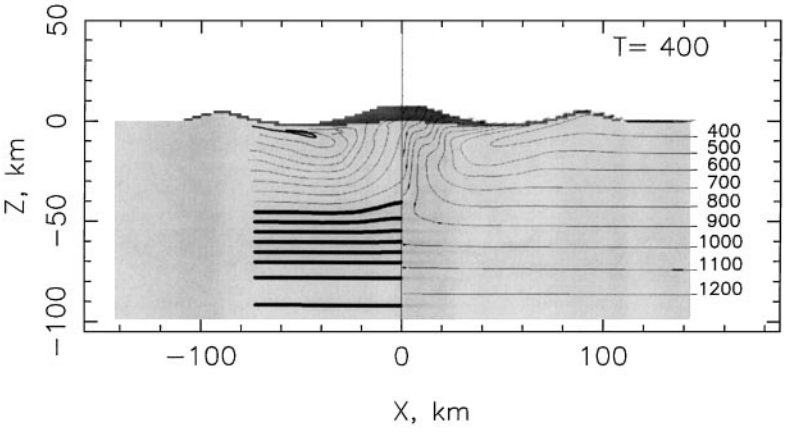
T= 400
Z, km
50
0
−50
−100
−100
0
100
X, km
400
500
600
700
800
900
1000
1100
1200

(c)

where erfc is the complementary error function, Ω is a dimensionless measure of the driving stress, and $\Omega = \tau/\tau_{static}$, where $\tau_{static} = \mu p$ is the stress required to initiate failure when no vibrations are present. Ω ranges from 0 to 1. Σ is a dimensionless measure of the amplitude of the vibrations $\Sigma = \sigma/p$. A somewhat more compact way to represent this flow law is to combine the dimensionless expression into one term, $X = (1 - \Omega)/\Sigma$.

$$\dot{\varepsilon} = \frac{\tau}{\rho\lambda\beta}\left\{\frac{2}{\mathrm{erfc}(X)} - 1\right\}^{-1} \tag{3b}$$

where X ranges from 1 to 0. The utility of this expression will be seen when we compare it with the block model.

The behavior of this rheological law is shown in Figure 3, where Equation 3b is plotted versus the dimensionless driving stress Ω. Although the strain rate is finite for any $\Omega > 0$, the strain rate becomes large only for $\Omega > (1-\Sigma)$, thus exhibiting a kind of Bingham yield behavior in which the yield stress is a function of the amplitude of shaking Σ. As the driving stress approaches the static limit $\Omega = 1$, the strain rate approaches a constant value $\dot{\varepsilon} = \tau_{static}/\rho\lambda\beta$. The stress-strain rate curve is otherwise complex and exhibits substantial non-Newtonian curvature. Complex as this flow law may seem, it has recently received experimental verification in a laboratory study of vibrated sand (Melosh & Girdner 1995).

The original model of acoustic fluidization was entirely a continuum model: the lengths of the elastic waves were assumed to be larger than any intact rock fragments in the material. A fundamental limitation of this model is that it does not predict the wavelength of the vibrations dominating the flow and thus cannot be used to make quantitative predictions of the rheology of the material without further assumptions. The model also does not produce a Bingham rheology in a straightforward way, although it does predict a sharp increase in creep rate above a threshold that depends on the mean amplitude of the vibrations. Questions such as how strong the shaking is and how long it goes on after impact are

←

Figure 2 A hydrocode simulation of the Sudbury event using a modified version of the SALE code (Amsden et al 1980). A cylindrical projectile with height and diameter both equal to 12.5 km impacts the granite surface at a velocity of 20 km s^{-1}. Model friction coefficients, μ, are equal to (*a*) 0.25, (*b*) 0.125, and (*c*) 0.0625. Vertical (depth) and horizontal (radial distance) scales are in kilometers. The axis of symmetry (zero radial distance) divides each frame in two halves. (*left*) Distortion and displacement of originally horizontal marked layers are shown in the target at $T = 400$ s. Thick lines correspond to layers below 45 km—an estimated Moho depth. The dark gray tone marks cells with densities less than 2000 kg m^{-3} but above 200 kg m^{-3}. (*right*) Displacement and distortion of the isotherms are shown. Isotherms are labeled in kelvins. After Ivanov & Deutsch (1998).

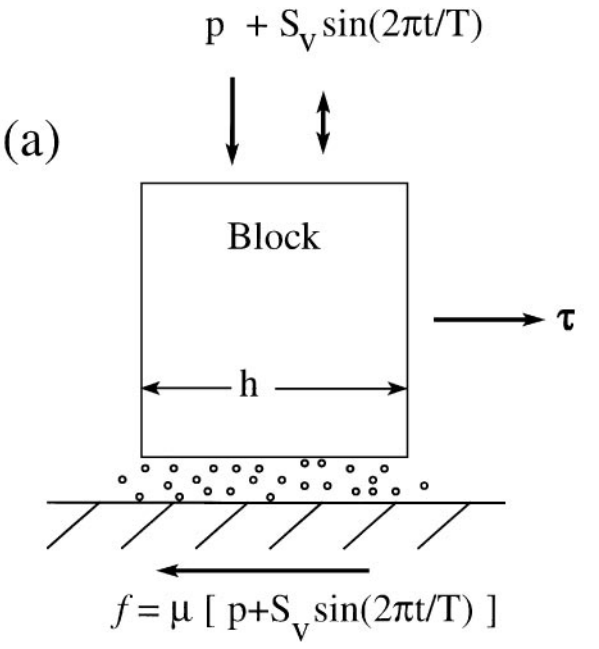
p + S_v sin(2πt/T)
(a)
Block
τ
h
f = μ [p+S_v sin(2πt/T)]

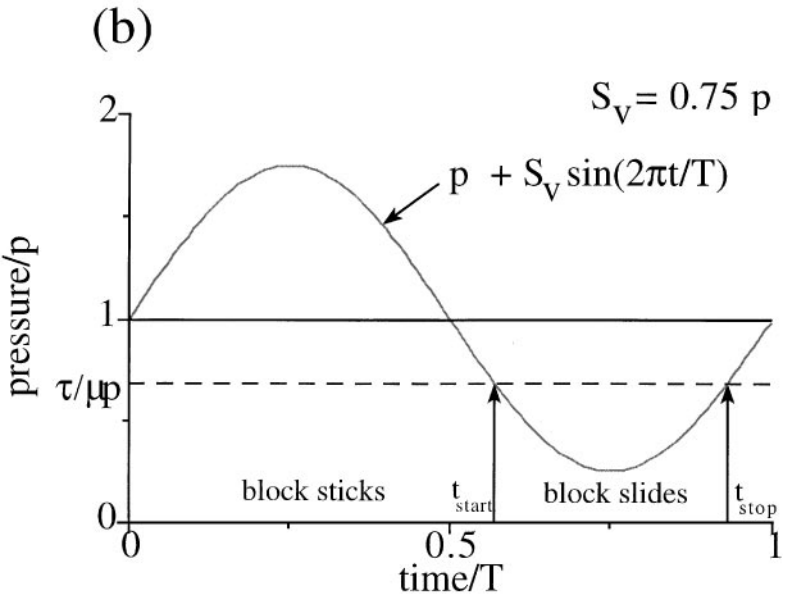
(b)
S_v = 0.75 p
p + S_v sin(2πt/T)
pressure/p
2
1
τ/μp
0
block sticks
t_start
block slides
t_stop
0
0.5
1
time/T

important for estimating the degree of collapse of the crater, but previous theories gave little information on these parameters. More recent studies (Melosh 1996) provide a rationale, still within the context of a continuum model, for estimating the rate at which acoustic (vibrational) energy in a mass of rock debris is generated, propagates elsewhere, and decays. In the future we hope that such modeling, carried out in conjunction with hydrocode computations, may yield deeper insight into how sub–mesh-scale vibrations might affect the gross strength properties of rock debris in the vicinity of an impact.

Block Model

One of the characteristic features of rock deformation is that the rock medium deforms not as a plastic metallike continuum but as a system of discrete rock blocks. Deep drilling of 40 km-scale impact craters reveals a system of rock blocks ranging in size from 50 to 200 m, with an average size of about 100 m (Ivanov et al 1996). A model of these block oscillations may be used to formulate an appropriate rheological law for the subcrater flow during the modification stage.

For this model to be valid, the time for sound to cross a block must be short compared with the period of vibration of one block against another. In other words, the sound speed of the matrix between the blocks must be much smaller than that of the intact rock. A soft interblock breccia layer of about 10 to 20 percent of the block's thickness (10–30 m) with a sound speed approximately 500 to 1000 m s^{-1} provides a plausible rationale for this model.

In a simple, one-dimensional approximation, the "acoustic fluidization" equations describe a single block sliding along the surface (Figure 3*a*). Imagine that the block is under a normal stress p that creates a dry friction force μp. This force prevents the block from moving under the traction stress τ. Let the block oscillate vertically with a period T. The oscillation creates a sinusoidal variation of the normal stress with amplitude S_v. Under this assumption the block is static (velocity $v = 0$) whenever the vertical stress $p + S_v \sin(2\pi t/T)$ creates a friction force larger than the traction. However, for the time period t_{free} (see Figure 4*b*), friction is less than the traction, and the block begins to move ($v > 0$). A minimal requirement for this motion is that $\tau > \mu(p - S_v)$, a condition which defines a kind of Bingham yield stress, $Y_B = \mu(p - S_v)$. If τ is

←

Figure 3 (*a*) Schematic drawing of the one-dimensional model for a block sliding along the underlying surface. The block, of size h, is under a static pressure p and a traction stress τ. The friction stress is proportional to the overburden pressure with a friction coefficient μ. The pressure oscillates around its static value p with amplitude S_v. (*b*) Time variation of the normal stress. Owing to oscillations, the friction force is below the strength limit during the period t_{free}. During this time the block accelerates under the applied traction. See text for a more detailed description.

less than Y_B, the block does not slide. If τ is greater than this threshold, there is a time during the cycle when the block is accelerated by the difference between the traction stress τ and the frictional resistance $\mu[p + S_v \sin(2\pi t/T)]$. When the normal stress increases back to the friction limit, the block stops. Figure 4*b* shows that this occurs between the third and fourth quadrant of the sine function at times given by

$$t_{start,stop} = \frac{T}{2\pi} \sin^{-1}\left(\frac{\tau - \mu p}{\mu S_v}\right) \tag{4}$$

During the next period of oscillation, the block moves again. This simple scheme allows us to construct a nonlinear rheological law similar to the acoustic fluidization equations proposed by Melosh (1979).

By integrating the acceleration and velocity of the block to obtain its displacement δ per cycle, it is easy to show that the strain rate of the block is given by $\dot{\varepsilon} = \delta/Th$ where h is a characteristic dimension of the block. The

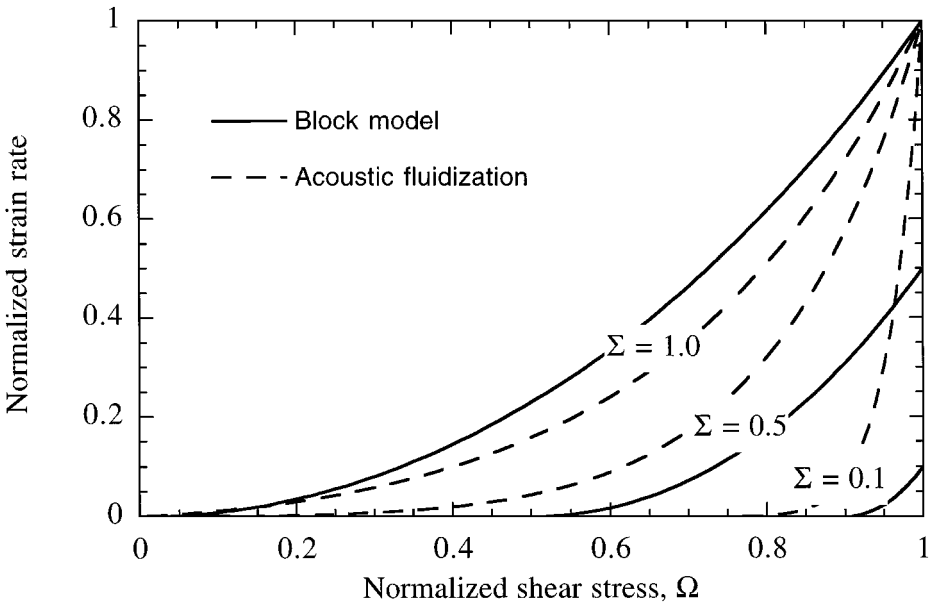

Figure 4 Rheologies of the original acoustic fluidization model and the block model for the flow of strongly vibrated rock debris. The plot illustrates the relation between strain rate, normalized by the maximum strain rate, and applied stress, normalized by the static sliding stress derived from Equations 3b and 5 in the text. The different curves are labeled by Σ, the dimensionless ratio between the amplitude of the vibrations and the overburden pressure. Although the two models differ in detail, their predictions for the rheology of strongly shaken rock debris are quite similar overall.

integration to derive δ yields a complex functional form, but the overall behavior is simply described. In analogy to Equation 3b the block model yields the rheological law

$$\dot{\varepsilon} = \frac{(\tau - Y_B)T}{2\pi^2 \rho h^2} \left\{ \sqrt{\frac{1+X}{1-X}} - \frac{X}{1-X} \cos^{-1} X \right\} \cos^{-1} X \tag{5}$$

where in this case $\Sigma = S_v/p$ and $X = (1 - \Omega)/\Sigma$, as before. Equation 5 applies to a model in which the block velocity drops to zero as soon as the frictional force exceeds the driving force. A more sophisticated numerical treatment accounts for inertial sliding for a short time after this, but the results differ little from Equation 5.

Figure 4 shows that this implies a rheological behavior very similar to that of acoustic fluidization. The maximum strain rate occurs when $\Omega = 1, \dot{\varepsilon} = (\tau_{static} - Y_B)T/(4\pi\rho h^2)$. Because Y_B is a function of the amplitude of vibration, the maximum strain rate depends on Σ, unlike the case for acoustic fluidization. There is a true Bingham threshold: flow does not begin until τ exceeds Y_B. After yielding, it flows with an effective viscosity given by $2\pi h^2/\rho T$. In spite of these differences the two flow laws are very similar because the ultimate fluidization mechanisms are quite similar. An advantage of the block model is that the length scale h is determined from an observable, whereas in the acoustic fluidization model the wavelength λ was undetermined. On the other hand, the block model itself does not define the period T of the dominant vibrations, which must be determined from other assumptions or observations.

Numerical Modeling: Central Peak, Double Ring

Ivanov and Kostuchenko (1997) published an example of numerical cratering simulations with a simplified acoustic fluidization model. The one-dimensional block oscillation model was implemented in a MAC-type free-surface Lagrangian numerical code (Welsh et al 1966). To simplify the model, they assumed initial conditions of a hemispherical transient crater cavity with initially flat layers deformed in accordance with the Z-model kinematic description of cratering (Maxwell 1977). The initial block oscillation intensity (measured as the amplitude of the velocity of a block oscillation) is assumed to be a constant fraction of the particle velocity behind the shock front (calculated with another type of a hydrocode). The oscillation intensity decays spatially as the inverse square of the distance from the impact point. The oscillation's decay in time follows an exponential law.

To define the scaling law, the block size was assumed to be proportional to the transient crater diameter. The quality factor Q for the oscillation's decay was assumed to be the same for all crater diameters. By definition, Q is the ratio between the energy stored per cycle and the energy lost over the same period. The frequency of the block oscillation needs to be in the range of several hertz,

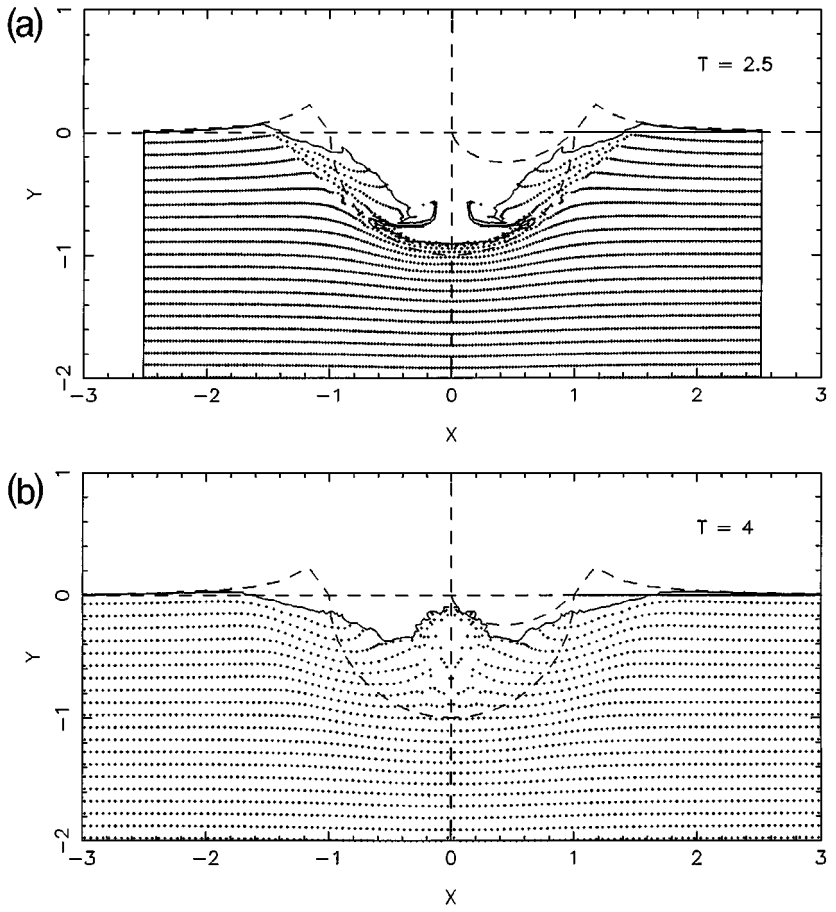

Figure 5 The final shape of collapsed craters with a diameter of ~2 km (*a*), ~20 km (*b*), ~40 km (*c*), and ~80 km (*d*) in the terrestrial gravity field. *Dashed lines* show the initial contour of the transient cavity and (*right*) the ejected volume. Initially flat layers (*dotted lines*) were distorted according to the Z model to form the transient cavity and then followed the crater collapse motion. The length unit is equal to the maximum transient cavity depth. The time unit is equal to the free-fall time from a height equal to the transient cavity radius, $(H_f/g)^{0.5}$.

and Q needs to be of the order of 10 to 100 to fit the observed crater profile. With these parameters we calculated the collapse of various size craters to study the morphology of the final crater. Selected results are shown in Figure 5, which illustrates the change of crater morphology with increasing crater diameter for complex craters.

The numerical computations are most efficiently done using nondimensional, or normalized, values for the viscosity and decay time parameters. Distances

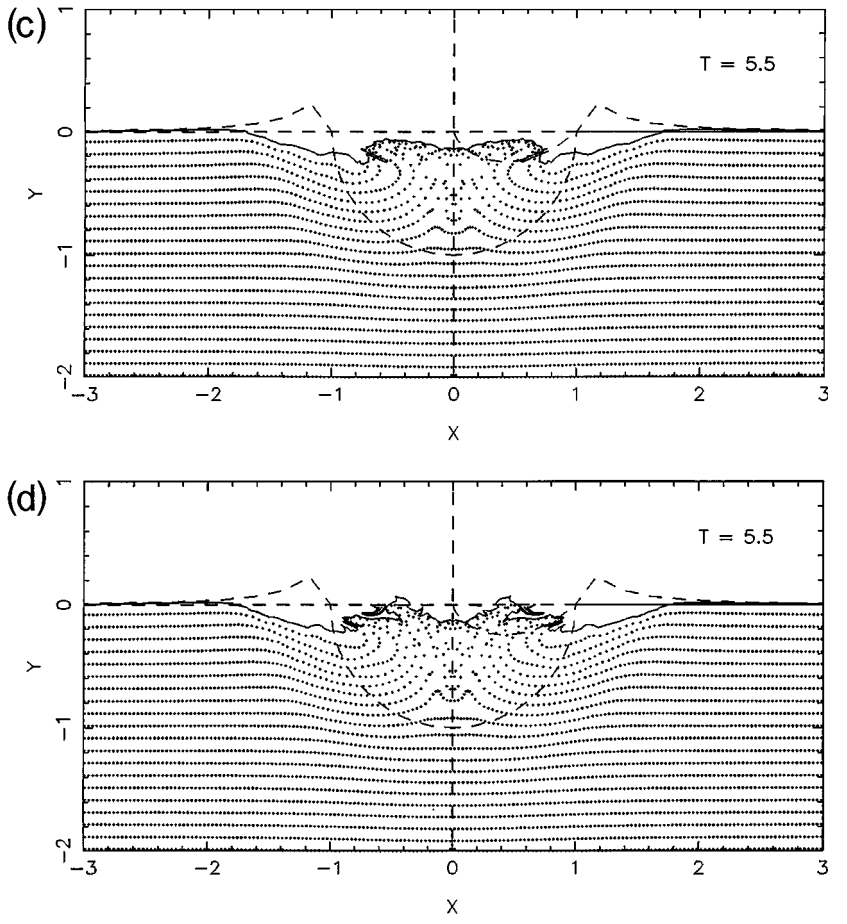

Figure 5 (*Continued*)

are normalized by the transient crater depth H_f. The normalized viscosity is $\eta^* = \eta\sqrt{H_f^3/g}$ and the normalized oscillation decay time is $t^* = t\sqrt{H_f/g}$, where η and t are the dimensional viscosity and decay time, respectively. The numerical computations indicate that a good fit with observations can be achieved with $\eta^* = 0.028$ and $t^* = 1.4$. For a 10 km-deep crater this corresponds to an actual viscosity of 2.4×10^8 Pa, an oscillation decay time of 45 seconds, and Q in the range of 10 to 200, depending somewhat on the assumed block size and the elastic modulus of the block system. For a Q of 10 the block size needs to be about 300 m, whereas a Q of 200 corresponds to 70 m blocks.

In small craters the rapid decay of the vibrations prevents floor uplift, and only a simple inward sliding of the crater walls modifies the transient cavity. Only for crater diameters above a critical threshold do block oscillations facilitate uplift of the crater floor before the prominent wall sliding. This uplift creates a central mound. The model approximately reproduces the well-known depth/diameter law for complex craters: the maximum depth of the final collapsed crater, d, grows with the final crater rim diameter, D, as $d \sim D^{1/3}$.

In this simulation the central uplift for very large craters experiences a substantial overshoot—the upper part of the growing central mound lifts well above the pre-impact ground level, then falls down before finally coming to rest. As the size of the modeled event increases, the further subsidence of the central mound following the overshoot begins to produce a pit at the top of the central uplift. The final topography strongly resembles a peak ring structure (Figure 5*d*). However, the resolution of the currently available numerical models is not yet high enough to permit quantitative analysis because the final model's topography is comparable with the size of computation cells.

The large block reformulation of the original Melosh acoustic fluidization model with proper parameterizations thus reproduces the main features of the impact crater collapse (*a*) the existence of a critical diameter below which no collapse occurs, and (*b*) a gradual change of crater morphology with increasing crater diameter.

The block size is an observable parameter, at least for terrestrial impact craters. Future work should incorporate some form of acoustic fluidization from the very beginning of transient crater growth. This may change the simple assumption of the hemispherical transient cavity used here.

CONCLUSIONS

Mechanical analysis of the collapse of impact craters has proved surprisingly difficult in comparison with the static analysis of the stability of big holes in the ground. Observations of impact crater collapse reveal that the dynamic strength properties of rock debris are strikingly different from their static properties. The very existence of a simple-complex crater transition requires the operation of some process that greatly degrades the strength of the material in the vicinity of an impact. This strength degradation is evidently transient, lasting little more than the few minutes required for craters in the 10 to 100 km range to collapse.

The study of large impact craters has thus revealed new and fundamental aspects of the behavior of Earth materials at scales much larger than we are accustomed to modeling in the laboratory. The information gleaned from studying impact crater collapse may have applications in other, apparently disparate, areas of Earth science. The physics of both earthquakes and long runout

landslides have aspects in common with that of collapsing impact craters (Melosh 1983). A deeper understanding of the formation of impact craters may thus have implications far outside the domain of cratering studies.

Within this domain, future progress in understanding the motions that occur in the target subsequent to a large impact will require numerical studies using increasingly sophisticated and realistic strength models. It will also require field and remote studies of impact craters to define better what really happens during collisions of very large Solar System objects.

ACKNOWLEDGMENTS

Boris Ivanov thanks the Russian Foundation for Basic Science for support of his work on impact cratering (grant 96-05-64167). Jay Melosh has been supported by NASA grant NAGW-428 of the Division of Planetary Geology and Geophysics.

Literature Cited

Alexopoulos JS, McKinnon WB. 1994. Large impact craters and basins on Venus, with implications for ring mechanics on the terrestrial planets. In *Large Meteorite Impacts and Planetary Evolution*, ed. BO Dressler, RAF Grieve, VL Sharpton, Spec. Pap. 293:29–50. Boulder, CO: Geol. Soc. Am.

Amsden AA, Ruppel HM, Hirt CW. 1980. *SALE: A Simplified ALE Computer Program for Fluid Flow at All Speeds*. *LA-8095, Los Alamos Natl. Lab*., Los Alamos, NM

Anderson CE. 1987. An overview of the theory of hydrocodes. *Int. J. Impact Eng.* 5:33–59

Asphaug E, Melosh HJ. 1993. The Stickney impact of Phobos: A dynamical model. *Icarus* 101:144–64

Baldwin RB. 1981. On the tsunami theory of the origin of multi-ring basins. See Schultz & Merrill 1981, pp. 275–88

Basilevsky AT, Ivanov BA, Florensky KP, Yakolev OI, Fel'dman VI, et al. 1983. *Impact Craters on the Moon and Other Planets*. Moscow: Nauka. 200 pp. (Engl. tech. transl. 1985. *NASA TM 77667*)

Bingham EC. 1916. An investigation of the laws of plastic flow. *Bull. Bur. Stand.* 13:309–53

Cooper HF, Sauer FM. 1977. Crater-related ground motions and implications for crater scaling. See Roddy et al 1977, p. 1245–60

Crandall SH, Mark WD. 1973. *Random Vibration in Mechanical Systems*. New York: Academic. 166 pp.

Dabija AI, Ivanov BA. 1978. Geophysical model of meteorite craters and some problems of cratering mechanics. *Meteoritika* 37:160–67. In Russian

Dade WB. 1998. Long runout rockfalls. *Geology* 26:803–6

Dence MR. 1965. The extraterrestrial origin of Canadian craters. *Ann. NY Acad. Sci.* 123:941–69

Dence MR, Grieve RAF, Robertson PB. 1977. Terrestrial impact structures: Principal characteristics and energy considerations. See Roddy et al 1997, p. 247–75

Dent B. 1973. Gravitationally induced stresses around a large impact crater. *EOS* 54:1207

Fourney WL, Holloway DC, Barker DB. 1984. Model studies of fragmentation. In *Mechanics of Oil Shale*, ed. KT Chang, JW Smith, p. 337–88. New York: Elsevier

Gaffney ES, Melosh HJ. 1982. Noise and target strength degradation accompanying shallow-buried explosions. *J. Geophys. Res.* 87:1871–79

Gilbert GK. 1893. The moon's face: A study of the origin of its features. *Bull. Philos. Soc. Wash.* 12:241–92

Grieve RAF, Dence MR, Robertson PB. 1977. Cratering processes: As interpreted from the occurrence of impact melts. See Roddy et al 1977, p. 791–814

Grieve RAF, Garvin JB. 1984. A geometric model for excavation and modification at

terrestrial simple craters. *J. Geophys. Res.* 89:11561–72
Grieve RAF, Robertson PB, Dence MR. 1981. Constraints on the formation of ring impact structures. See Schultz & Merrill 1981, p. 37–57
Grieve RAF, Shoemaker EM. 1994. Record of past impacts on Earth. In *Hazards Due to Comets and Asteroids*, ed. T Gehrels, p. 417–62. Tucson: Univ. Ariz. Press
Hartmann WK, Kuiper GP. 1962. Concentric structures surrounding lunar basins. *Commun. Lunar Planet. Lab.* Tucson: Univ. Ariz. 1:51–66
Holsapple KA, Schmidt RM. 1982. On the scaling of crater dimensions–2. Impact processes. *J. Geophys. Res.* 87:1849–70
Ivanov BA, Basilevsky AT, Sazonoya LV. 1982. Formation of the central uplift in meteoritic craters. *Meteoritika* 40:60–81. In Russian. (Engl. tech. transl. 1986. *NASA TM-88427*)
Ivanov BA, Deniem D, Neukum G. 1997. Implementation of dynamic strength models into 2D hydrocodes: Applications for atmospheric breakup and impact cratering. *Int. J. Impact Eng.* 20:411–30
Ivanov BA, Deutsch A. 1998. Sudbury impact event: Cratering mechanics and thermal history. In *Proc. Sudbury Conf.*, ed. Dessler. Houston: Lunar Planet. Inst. In press
Ivanov BA, Kocharyan GG, Kostuchenko VN, Kirjakov AF, Pevzner LA. 1996. Puchezh-Katunki impact crater: Preliminary data on recovered core block structure. *Lunar Planet. Sci. Conf.* 27:589–90
Ivanov BA, Kostuchenko VN. 1997. Block oscillation model for impact crater collapse. In *Lunar Planet. Sci. Conf. 27th, Abstr. 1655*. Houston: Lunar Planet. Inst. (CD-ROM)
Ivanov BA, Kostuchenko VN. 1998. Impact crater formation: Dry friction and fluidization influence on the scaling and modification. In *Lunar Planet. Sci. Conf. 29th, Abstr. 1654*. Houston: Lunar Planet. Inst. (CD-ROM)
Ivanov BA, Nemchinov IV, Svetsov VA, Provalov AA, Khazins VM, Phillips RJ. 1992. Impact cratering on Venus: Physical and mechanical models. *J. Geophys. Res.* 97: 16167–81
Jaeger JC, Cook NGW. 1969. *Fundamentals of Rock Mechanics*. London: Chapman & Hall. 515 pp.
Johnson WE, Anderson CE. 1987. History and application of hydrocodes in hypervelocity impact. *Int. J. Impact Eng.* 5:423–39
Leith AC, McKinnon WB. 1991. Terrace width variations in complex Mercurian craters, and the transient strength of the cratered Mercurian and lunar crust. *J. Geophys. Res.* 96:20923–31
Masaitis VL, Danilin AN, Maschak MS, Raikhlin AI, Selivanovskaya TV, Schadenkov EM. 1980. *Geology of Astroblems*. Leningrad: Nedra. 231 pp. In Russian
Maxwell DE. 1977. A simple model of cratering, ejection, and the overturned flap. See Roddy et al 1977, pp. 1003–8
McKinnon WB. 1978. An investigation into the role of plastic failure in crater modification. *Proc. Lunar Planet. Sci. Conf.* 9:3965–73
McKinnon WB, Melosh HJ. 1980. Evolution of planetary lithospheres: Evidence from multiringed basins on Ganymede and Callisto. *Icarus* 44:454–71
McKinnon WB, Zahnle KJ, Ivanov BA, Melosh HJ. 1997. Cratering on Venus: Models and observations. In *Venus II*, ed. SW Bougher, DM Hunten, RJ Phillips, pp. 969–1014. Tucson: Univ. Ariz. Press
Melosh HJ. 1977. Crater modification by gravity: A mechanical analysis of slumping. See Roddy et al 1977, p. 1245–60
Melosh HJ. 1979. Acoustic fluidization: A new geologic process? *J.Geophys. Res.* 84:7513–20
Melosh HJ. 1982a. A schematic model of crater modification by gravity. *J. Geophys. Res.* 87:371–80
Melosh HJ. 1982b. A simple mechanical model of Valhalla Basin, Callisto. *J. Geophys. Res.* 87:1880–90
Melosh HJ. 1983. Acoustic fluidization. *Am. Sci.* 71:158–65
Melosh HJ. 1985. Impact cratering mechanics: Relationship between the shock wave and excavation flow. *Icarus* 62:339–43
Melosh HJ. 1989. *Impact Cratering: A Geologic Process*. New York: Oxford Univ. Press. 245 pp.
Melosh HJ. 1996. Dynamic weakening of faults by acoustic fluidization. *Nature* 379:601–6
Melosh HJ, Gaffney ES. 1983. Acoustic fluidization and the scale dependence of impact crater morphology. *J. Geophys. Res.* 88(Suppl. A):830–34
Melosh HJ, Girdner KK. 1995. Rheology of vibrated granular materials: Application to long runout landslides (Abs). *Eos* 76 (Suppl. F):270
Melosh HJ, McKinnon W. 1978. The mechanics of ringed basin formation. *Geophys. Res. Lett.* 5:985–88
Moore HJ. 1976. Missile impact craters (White Sands Missile Range, New Mexico) and applications to lunar research. *US Geol. Surv. Prof. Pap. 812-B*
Morgan J, Warner M, Group TCW. 1997. Size and morphology of the Chicxulub impact crater. *Nature* 390:472–76

Nolan MC, Asphaug E, Melosh HJ, Greenberg R. 1996. Impact craters on asteroids: Does strength or gravity control their size? *Icarus* 124:359–71

O'Keefe JD, Ahrens TJ. 1993. Planetary cratering mechanics. *J. Geophys. Res.* 98:17011–28

O'Keefe JD, Ahrens TJ. 1998. Complex craters: Relationship of stratigraphy and rings to the impact conditions. *J. Geophys. Res.* In press

Onorato PIK, Uhlmann DR, Simonds CH. 1978. The thermal history of the Manicouagan impact melt sheet, Quebec. *J. Geophys. Res.* 83:2789–98

Passey QR, Shoemaker EM. 1982. Craters and Basins on Ganymede and Callisto: Morphological indicators of crustal evolution. In *Satellites of Jupiter*, ed. D Morrison, MS Matthews, pp. 379–434. Tucson: Univ. Ariz. Press

Pearce SJ, Melosh HJ. 1986. Terrace width variations in complex lunar craters. *Geophys. Res. Lett.* 13:1419–22

Pike RJ. 1977. Size dependence in the shape of fresh impact craters on the Moon. See Roddy et al 1977, p. 489–509

Pike RJ. 1980. Control of crater morphology by gravity and target type: Mars, Earth, moon. *Proc. Lunar Planet. Sci. Conf.* 11:2159–89

Quaide WL, Gault DE, Schmidt RA. 1965. Gravitative effects on lunar impact structures. *Ann. NY Acad. Sci.* 123:563–72

Roddy DJ, Boyce JM, Colton GW, Dial AL. 1975. Meteor Crater, Arizona, rim drilling with thickness, structural uplift, diameter, depth, volume, and mass-balance calculations. *Proc. Lunar Sci. Conf.* 6:2621–44

Roddy DJ, Pepin RO, Merrill RB, eds. 1977. *Impact and Explosion Cratering*. New York: Pergamon

Rodionov VN, Adushkin VV, Kostuchenko VN, Nikolaevsky VN, Romashov AN, et al. 1971. *Mechanical Effects of An Underground Explosion*. Moscow: Nedra. 221 pp. In Russian. (Engl. transl. 1972. *USAEC UCRL-Trans-10676*. Los Alamos, NM)

Schenk PM. 1991. Ganymede and Callisto: Complex crater formation and planetary crusts. *J. Geophys. Res.* 96:15635–64

Schenk PM. 1993. Central pit and dome craters: Exposing the interiors of Ganymede and Callisto. *J. Geophys. Res.* 98:7475–98

Schenk PM, McKinnon WB. 1987. Ring geometry on Ganymede and Callisto. *Icarus* 72:209–34

Schmidt RM, Housen KR. 1987. Some recent advances in the scaling of impact and explosion cratering. *Int. J. Impact Eng.* 5:543–60

Schultz PH, Merrill RB, eds. 1981. *Multiring Basins*. New York: Pergamon

Scott RF. 1967. Viscous flow of craters. *Icarus* 7:139–48

Seed HB, Goodman RE. 1964. Earthquake stability of slopes of cohesionless soils. *Proc. Am. Soc. Civ. Eng.* 90 (SM-6):43–73

Shoemaker EM. 1963. Impact mechanics at Meteor Crater, Arizona. In *The Moon, Meteorites and Comets*, ed. BM Middlehurst, GP Kuiper, 4:301–36. Chicago, IL: Univ. Chicago Press

Spray JG, Thompson LM. 1995. Friction melt distribution in a multi-ring impact basin. *Nature* 373:130–32

Spudis PD. 1993. *The Geology of Multi-Ring Impact Basins*. Cambridge, UK: Cambridge Univ. Press 263 pp.

Thomas PC, Binzel RP, Gaffey MJ, Storrs AD, Wells EN, Zellner BH. 1997. Impact excavation on asteroid 4 Vesta: Hubble Space Telescope results. *Science* 277:1492–95

Ullrich GW, Roddy DJ, Simmons G. 1977. Numerical simulations of a 20-ton TNT detonation on the Earth's surface and implications concerning the mechanics of central uplift formation. See Roddy et al 1977, p. 959–82

Welsh JE, Harlow FH, Shannon JP, Daly BJ. 1966. The MAC method. A computing technique for solving viscous, incompressible, transient fluid-flow problems involving free surfaces. *Tech. Rep. TID-4500, Los Alamos Sci. Lab*., Los Alamos, NM. 146 pp.

Wieczorek MA, Phillips RJ. 1999. Lunar multiring basins and the cratering process. *Icarus* (In press)

Wood CA, Head JW. 1976. Comparison of impact basins on Mercury, Mars and the Moon. *Proc. Lunar Planet. Sci. Conf.* 7:3629–51

Worthington AM. 1963. *A Study of Splashes*. New York: Macmillan. 169 pp.